Materials Today Bio 10 (2021) 100087

Contents lists available at ScienceDirect

Materials Today Bio

journal homepage: www.journals.elsevier.com/materials-today-bio

A two-in-one Janus NIR-II AIEgen with balanced absorption and emission for image-guided precision surgery

S. Liu [a], Y. Li [a], J. Zhang [a], H. Zhang [a], Y. Wang [a], C. Chuah [c], Y. Tang [c], J.W.Y. Lam [a], R.T.K. Kwok [a], H. Ou [b,**], D. Ding [b], B.Z. Tang [a,d,e,*]

[a] Department of Chemistry, Hong Kong Branch of Chinese National Engineering Research Center for Tissue Restoration and Reconstruction, Division of Life Science and State Key Laboratory of Molecular Neuroscience, Division of Biomedical Engineering, The Hong Kong University of Science and Technology, Clear Water Bay, Kowloon, Hong Kong, China

[b] Key Laboratory of Bioactive Materials Ministry of Education and College of Life Sciences, Nankai University, Tianjin, 300071, China

[c] Institute for NanoScale Science and Technology, College of Science and Engineering, Flinders University, South Australia, 5042, Australia

[d] Center for Aggregation-Induced Emission SCUT-HKUST Joint Research Institute State Key Laboratory of Luminescent Materials and Devices South China University of Technology, Guangzhou, 510640, China

[e] AIE Institute, Guangzhou Development District, Huangpu, Guangzhou, 510530, China

ARTICLE INFO

Keywords:
Aggregation-induced emission
Fluorescence
Image-guided surgery
Absorbance
Brightness

ABSTRACT

Fluorescence imaging in the near-infrared II (NIR-II, 1000–1700 nm) region opens up new avenues for biological systems due to suppressed scattering and low autofluorescence at longer-wavelength photons. Nonetheless, the development of organic NIR-II fluorophores is still limited mainly due to the shortage of efficient molecular design strategy. Herein, we propose an approach of designing Janus NIR-II fluorophores by introducing electronic donors with distinct properties into one molecule. As a proof-of-concept, fluorescent dye 2 TT-*m*, *o*C6B with both twisted and planar electronic donors displayed balanced absorption and emission which were absent in its parent compound. The key design strategy for Janus molecule is that it combines the merits of intense absorption from planar architecture and high fluorescence quantum yield from twisted motif. The resulting 2 TT-*m*, *o*C6B nanoparticles exhibit a high molar absorptivity of 1.12 ×10^4 M^{-1} cm^{-1} at 808 nm and a NIR-II quantum yield of 3.7%, displaying a typical aggregation-induced emission (AIE) attribute. The highly bright and stable 2 TT-*m*, *o*C6B nanoparticles assured NIR-II image-guided cancer surgery to resect submillimeter tumor nodules. The present study may inspire further development of molecular design philosophy for highly bright NIR-II fluorophores for biomedical applications.

1. Introduction

Cancer is responsible as the leading cause of death globally [1]. Tumor detection at an early stage is crucial for a successful treatment. Although advances have been made in traditional diagnostic methodologies, such as magnetic resonance imaging, computed tomography and positron emission tomography, they do not attain the required sensitivity and specificity for detecting the disease at an early-stage [2,3]. Fluorescence imaging-guided cancer surgery has been demonstrated clinically to detect tiny tumor foci or the exact borders between normal and tumor tissues during surgery owing to its high sensitivity, real-time capability, absence of ionizing radiation and portability [4,5]. Fluorophores emitting in the near-infrared II (NIR-II, 1000–1700 nm) region have received increasing attention because of their merits for having increased tissue penetration, improved spatial resolution and high signal-to-background ratio [6–15]. To date, outstanding achievements have been obtained by inorganic materials, attaining enhanced brightness for biomedical applications [16–20]. However, these inorganic materials generally suffer from potentially long-term toxicity. Alternatively, organic materials with the advantages of good biocompatibility, potential biodegradability and excellent processibility are promising for NIR-II bioimaging [21–27]. However, the molecular design philosophy for organic NIR-II fluorophores is not widely reported, as traditional methods rely on trial and error via extensive tuning of chemical structures with promising motifs. Thereof, a convenient yet efficient molecular design strategy for highly efficient NIR-II fluorophores is fascinating.

* Corresponding author.
** Corresponding author.
E-mail addresses: hlou@nankai.edu.cn (H. Ou), tangbenz@ust.hk (B.Z. Tang).

https://doi.org/10.1016/j.mtbio.2020.100087
Received 3 October 2020; Received in revised form 23 November 2020; Accepted 25 November 2020
Available online 3 December 2020

It is widely accepted that increasing the length of π-conjugation and engineering donor-acceptor (D-A) units can efficiently shift the fluorescence emission toward the long-wavelength region [28–31]. These molecules are typically featured with planar architectures to exhibit strong absorption and emission signals as isolated species. However, when they are dispersed in biological medium (water), the resultant intense intermolecular π–π interactions often quench the fluorescence [32]. Such aggregation-caused quenching (ACQ) effects make them unsuitable for bioimaging applications, which may give false feedback on tumor diagnosis. As a technology related to aggregate-state luminescence, aggregation-induced emission (AIE) holds the potential to tackle this issue [33–38]. AIE luminogens (AIEgens) commonly own twisted structures that can efficiently suppress intermolecular interactions, resulting in improved fluorescence in the aggregated state [39–42]. However, the twisted architecture blue-shifts the absorption peak, which hinders the laser excitation for deep tissue imaging in biological applications. Therefore, it remains challenging to develop NIR-II fluorophores with maximum absorption at longer wavelengths with high fluorescence quantum yield (QY).

Herein, we propose a molecular design strategy of developing Janus NIR-II fluorophores through tethering electronic donors with distinct properties into acceptors to attain fluorophores with two-in-one photophysical properties. As a proof-of-concept, as shown in Fig. 1, by combining the planar donor from ACQ-dominated 2TT-*m*C6B and twisted donor from AIE-active 2TT-*o*C6B, the newly formed molecule 2TT-*m, o*C6B possessed both planar and twisted donors. As a consequence of such molecular design, 2TT-*m, o*C6B displayed a typical AIE attribute due to the restriction of intermolecular interactions by the twisted donor. Compared to 2TT-*o*C6B, 2TT-*m, o*C6B showed a 54 nm redshift in absorption peak (750 nm) with an emission peaked at 1059 nm. Meanwhile, the QY of 2TT-*m, o*C6B aggregate reached up to 3.7%, which was better than 2TT-*m*C6B (0.75%). Moreover, 2TT-*m, o*C6B showed an increased molar absorptivity ($1.12 \times 10^4\ M^{-1}\ cm^{-1}$) than that of 2TT-*o*C6B ($0.8 \times 10^4\ M^{-1}\ cm^{-1}$). As a result, the 2TT-*m, o*C6B nanoparticles (NPs) are promising for NIR-II fluorescence imaging, which outperforms the clinically approved dye. Given the high brightness, the 2TT-*m, o*C6B NPs can act as an effective fluorescent agent for tumor imaging-guided surgery to resect tiny tumor modules that are indistinguishable to surgeons. The present study may inspire some insights into the molecular design philosophy of highly bright NIR-II dyes for biomedical applications.

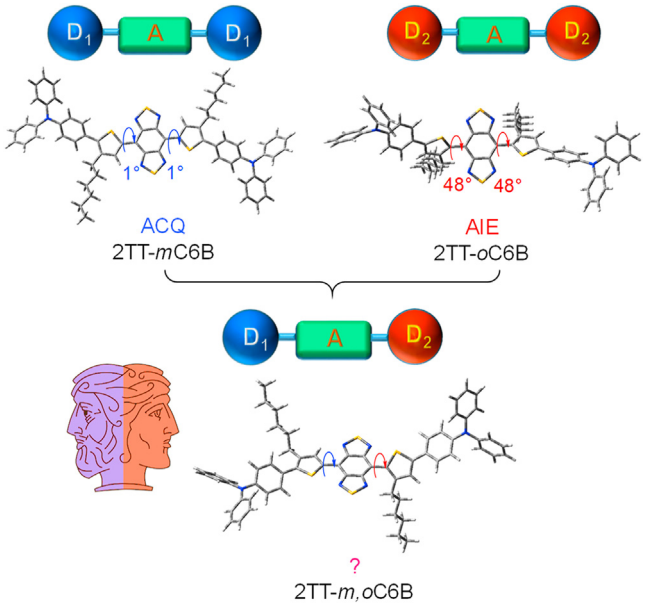

Fig. 1. Combination of 2TT-*m*C6B with 2 TT-*o*C6B to yield Janus dye 2TT-*m,o*C6B.

2. Materials and methods

2.1. Fabrication of 2TT-m, oC6B NPs

A mixture of 2TT-*m, o*C6B (1 mg), DSPE-PEG_{2000} (1.5 mg) and THF (1 mL) was sonicated (12 W output, XL2000, Misonix Incorporated, NY) to obtain a clear solution. The mixture was quickly injected into 9 mL of water, which was sonicated vigorously in water for 2 min. The mixture was stirred in fume hood for 12 h to remove the THF. The 2TT-*m, o*C6B NPs suspension was performed for ultrafiltration (molecule weight cutoff 100 kDa) at 3000 g for 30 min.

2.2. NIR-II fluorescence imaging setup

Imaging was carried out on a home-built imaging setup consisting of a 2D InGaAs camera (Princeton Instruments, 2D OMA-V). The excitation source was an 808 nm laser. The power density of the excitation laser at the imaging plane was 20 mW/cm^2, significantly lower than the reported safe exposure limit of 329 mW/cm^2 at 808 nm, which is indicated by the International Commission on Non-Ionizing Radiation Protection guidelines to avoid the laser-induced retinal injury [43,44].

2.3. In vitro NIR-II fluorescence imaging of 2TT-m, oC6B NPs and ICG

The NIR-II fluorescence imaging system was applied to collect the NIR-II fluorescent signals of 2TT-*m, o*C6B NPs and ICG (100 μM based on 2TT-*m, o*C6B and ICG, ICG was dispersed in double-distilled water) using different long-pass (LP) filters (1000, 1100, 1250 nm) under 808 nm irradiation (1000 nm, 50 ms; 1100 nm, 100 ms; 1250 nm, 200 ms).

2.4. Cell culture

4T1 breast cancer cells and luciferase-expressed 4T1 cancer cells were cultured in the DMEM containing 10% FBS and antibiotics (100 units/mL penicillin and 100 g/mL streptomycin) in a 5% CO_2 humidity incubator at 37 °C.

2.5. In vitro cytotoxicity study

MTT assays were employed to evaluate the cytotoxicity of 2TT-*m, o*C6B NPs against 4T1 cancer cells. In brief, 4T1 cells were seeded in 96-well plates at a density of 5×10^3 cells per well. After 24 h incubation, the cells were exposed to a series of doses (0, 1, 5, 10 and 25 μM based on 2TT-*m,o*C6B) of 2 TT-*m, o*C6B NPs. After incubated for another 24 h, the wells were washed with 1 × PBS buffer and 100 μL of freshly prepared MTT solution (0.5 mg/mL) in culture medium was added into each well. The MTT medium solution was carefully removed after 4 h incubation in the incubator. DMSO (100 μL) was then added and the absorbance of MTT at 570 nm was then monitored by the microplate reader. Cell viability was expressed by the ratio of the absorbance of cells incubated with 2TT-*m, o*C6B NPs to that of the cells incubated with culture medium only.

2.6. Animals and tumor xenograft model

Spraque Dawley (SD) rats (rat weight ~200g, n = 3) were used in the investment of the pharmacokinetics of 2TT-*m, o*C6B NPs. C57BL/6J mice (mouse weight ~20g, n = 6) were used in *in vivo* NIR-II fluorescence imaging of blood vessels and biodistribution study. Balb/c mice (mouse weight ~20g, n = 12) were used in the assessment of *in vivo* toxicity of 2 TT-*m, o*C6B NPs. Balb/c nude mice (mouse weight ~20g, n = 3) were used in *in vivo* NIR-II fluorescence imaging of the lymphatic system. To establish the peritoneal carcinomatosis-bearing mouse model, a total of 800,000 luciferase-expressed 4T1 cancer cells suspended in PBS buffer

were intraperitoneally injected into the Balb/c mice (mouse weight ~20 g, n = 5). Small tumor nodules were formed and scattered in the mouse peritoneal cavity (most on the surface of the small intestine) after 5 days.

2.7. In vivo toxicity study

Healthy Balb/c mice were randomly assigned to 2 groups, namely, group I: control; group II: 2TT-*m, o*C6B NPs (each group contained 6 mice). On day 0, the mice in group II were intravenously injected with 200 μL of 2TT-*m, o*C6B NPs (1 mM based on 2TT-*m,o*C6B, injection dose (ID) = 10 mg/kg). A week later, the mice in two groups were sacrificed and the blood was collected through cardiac puncture at the time of sacrifice for blood chemistry analyses by Tianjin First Central Hospital.

2.8. In vivo pharmacokinetics study

After intravenous injection of 2TT-*m, o*C6B NPs (2 mL, 1 mM based on 2 TT-*m,o*C6B, ID = 10 mg/kg), the blood samples of SD rats (n = 3) were collected at predetermined time point (10 min, 30 min, 1 h, 2 h, 4 h, 8 h, 12 h and 24 h). After standing at room temperature for 0.5 h, the blood samples were centrifuged at 5000 rpm for 10 min to remove the blood cells. Subsequently, the plasma was collected and measured by a fluorescence spectrometer (excitation at 808 nm and emission at 1050 nm). The amount of 2 TT-*m, o*C6B NPs remaining in blood was determined according to its standard curve. The percent injected dose (%ID) was calculated by comparing the amount of 2TT-*m, o*C6B NPs remaining in blood with the injected dose. Blank samples from rats were analyzed as the background fluorescence of the plasma.

2.9. In vivo NIR-II fluorescence imaging of blood vessels

The NIR-II fluorescence of blood vessels in brain and hindlimb were imaged utilizing 1250 nm LP filter (exposure time: 500 ms). After intravenous injection of 2TT-*m, o*C6B NPs and ICG (200 μL, 1 mM based on 2 TT-*m, o*C6B and ICG) into C57BL/6J mice (n = 3 per group), respectively, the *in vivo* NIR-II fluorescence of blood vessels in brain and hindlimb were imaged at predetermined time points (5 min, 2 h, 4 h, 6 h, 8 h and 24 h).

2.10. Biodistribution study

The biodistribution of 2TT-*m, o*C6B NPs and ICG in mice were studied. After vascular imaging at 24 h post-injection of 2TT-*m, o*C6B NPs and ICG, respectively, the C57BL/6J mice (n = 3 per group) were sacrificed and their major tissues (heart, liver, spleen, lung, kidney and brain) were isolated and imaged (1250 nm LP filter, 500 ms).

2.11. NIR-II fluorescence image-guided surgery

At 12 h post-injection of 2TT-*m, o*C6B NPs (1 mM based on 2TT-*m,o*C6B, 200 μL) into the peritoneal carcinomatosis-bearing mice (n = 3) via the tail vein, D-luciferin suspended in PBS buffer was intraperitoneally injected into the peritoneal carcinomatosis-bearing mice; 5 min later, the mice were euthanatized and the abdomen cavity of mice was opened for bioluminescence and NIR-II fluorescence imaging. Bioluminescence imaging was performed using the Xenogen IVIS® Lumina II system, while the NIR-II fluorescence imaging was carried out using the home-built NIR-II imaging instrument (1250 nm LP filter, 500 ms). The tumor resection surgery was firstly performed by the experience of a surgeon without imaging guidance (unguided), followed by a second surgery to the same mice by the guidance of NIR-II fluorescence imaging. The excised tumor nodules were analyzed by both NIR-II fluorescence imaging and bioluminescence imaging. The tumor sizes resected from the first and second surgery were also quantified.

2.12. In vivo NIR-II fluorescence imaging of the lymphatic system

Before the experiments, adult nude mice (6–8 weeks old) were anesthetized with avertin (2,2,2-Tribromoethanol, 250 mg/kg, IP). After subcutaneous injection (1 mM based on 2TT-*m,o*C6B, 50 μL) of 2TT-*m, o*C6B NPs in the footpads, the lymphatic system of the Balb/c nude mice (n = 3) was imaged immediately at the predefined time points (1250 nm LP filter, 500 ms). At 24 h post-injection of AIEgen NPs, after carefully dissecting the superficial skin, the lymph nodes were dissected out by the guidance of NIR-II fluorescence imaging and imaged under bright field and 808 nm laser excitation conditions, respectively.

2.13. Histological study

Histological analysis of the excised tumor nodules and lymph nodes from the mice was performed by the surgeon. Briefly, the tissues were fixed in 4% paraformaldehyde, processed routinely into paraffin, sectioned at a thickness of 5 μm, and stained with hematoxylin and eosin (H&E). The slices were imaged by a digital microscope (Leica QWin).

2.14. Animal ethics

All animal experiments were performed in compliance with the guidelines set by Tianjin Committee of Use and Care of Laboratory Animals and the overall project protocols were approved by the Animal Ethics Committee of Nankai University. All the mice were obtained from Laboratory Animal Center of the Academy of Military Medical Sciences (Beijing, China).

2.15. Statistical analysis

Quantitative data were expressed as mean ± standard deviation. Statistical comparisons were made by ANOVA analysis and Student's t-test. P value < 0.05 was considered statistically significant.

3. Results and discussion

3.1. Molecular synthesis and design

The synthetic routes and characterization of the three molecules associated with intermediates were shown in the supplementary material [Scheme S1-3, Figs. S1-16)]. Traditionally, most NIR-II fluorophores are derived from D-A-D structures. In these molecules, benzobisthiadiazole (BBTD) is often employed as strong acceptors, whose stabilized quinoidal structure can redshift the emission to the NIR-II region [45–47]. Electron donors play decisive roles in the fluorescence properties of D-A-D fluorophores. For instance, 4-(2-thienyl) triphenylamine (TTA) moiety has been demonstrated as both electronic donor and π-conjugated bridge, which can couple with BBTD to afford long-wavelength emission [47, 48]. Through the introduction of alkyl chains to different positions of thiophene (T) unit, the resulting fluorophores can show distinct photophysical properties. As shown in Fig. 1, molecule 2TT-*m*C6B with a hexyl unit located on the 3-position of T displayed a coplanar T-BBTD-T structure (3-TBT, dihedral angle of 1°), owing to its useful conjugation.

On the one hand, the planar architecture gave 2TT-*m*C6B intense absorption in the long-wavelength range, which could not only penetrate deep tissues but also reduce photo-damage to the living body [47]. On the other hand, the planar structure also resulted in strong intermolecular π-π interactions in the aggregated state, giving undesirable ACQ effect. Alternatively, molecule 2TT-*o*C6B with a hexyl unit grafted on the 4-position of T displayed a distorted T-BBTD-T structure (4-TBT, dihedral angle of 48°), owing to the enhanced steric hindrance between BBTD core and alkyl chains [29]. The twisted backbone coupled with triphenylamine (TPA) rotor endowed 2TT-*o*C6B AIE attribute by efficient restriction of intramolecular interactions in the aggregated state. Notably, AIE-active 2TT-*o*C6B showed a high solid-state QY of 8.4%, which was

beneficial for bioimaging [29]. However, the distorted architecture broke the conjugation, resulting in an unsatisfactory blueshift in absorption. Collectively, these two molecular design strategies possessed advantages and disadvantages in fluorescence imaging. Can we integrate long-wavelength absorption and high QY into one molecule to attain a highly bright NIR-II fluorophore? To address this issue, we proposed a molecular design strategy of incorporating different donors into one molecule (denoted "Janus" molecule). The key design strategy for Janus molecule was to combine planar and twisted TTA moieties into BBTD core [Fig. 1]. The planar unit was expected to afford strong absorption in long-wavelength range, while the twisted counterpart was hoped to supply high QY in the aggregated state. The resultant two-in-one molecule 2TT-*m, o*C6B with balanced absorption and emission property may improve imaging quality in biological applications.

3.2. Theoretical calculation

In order to confirm the molecular conformation (Fig. 2a), density functional theory (DFT) calculations were performed using Gaussian 09 software. The dihedral angle between T and BBTD was 1° in the optimized ground-state (S_0) of 2TT-*m*C6B, while it was 48° in 2TT-*o*C6B (Fig. 2b). These results confirmed the important roles of alkyl chains in determining the molecular architectures [11]. Notably, the dihedral angles in Janus molecule 2TT-*m, o*C6B were 5° and 48° for 3-TBT and 4-TBT moieties, respectively, suggesting the adaption of a planar plus twisted architecture. It should be noted that the presence of twisted TPA unit can hardly affect the planarity of the core. This result demonstrated the feasibility of the present molecular design strategy. Fig. 2c shows the highest occupied molecular orbital (HOMO) and the lowest unoccupied molecular orbital (LUMO) of the molecules. The molecular HOMO was delocalized along the whole molecular backbone for the three dyes, while the LUMO location was different. For example, the LUMO in 2 TT-*m*C6B was localized on both central T-BBTD-T core and part of the TPA unit owing to the better conjugation. However, it was only located at the T-BBTD-T core for 2TT-*o*C6B because of the breakage in conjugation. Interestingly, the LUMO of 2TT-*m, o*C6B was located at both BBTD-T-TPA and BBTD-T units, precisely inheriting from its parents. Moreover, the energy gap between HOMO and LUMO in 2TT-*m, o*C6B was 1.35 eV, which was between 2TT-*m*C6B (1.24 eV) and 2TT-*o*C6B (1.47 eV). This narrow energy gap was favorable for strong absorption in the NIR biological region. Overall, all these data supported the success of the present strategy, demonstrating an accurate manipulation of the photophysical properties by structural modification.

3.3. Photophysical properties

Given the novel planar/twisted structure of 2TT-*m,o*C6B, the photophysical properties were compared with its parent compounds. As shown in Fig. 3a, the absorption maximum of 2TT-*m, o*C6B (750 nm) in tetrahydrofuran (THF) outperformed that of 2TT-*o*C6B (696 nm), indicating that introduction of the planar unit was beneficial for redshifting the absorption [28]. Meanwhile, the blueshift of absorption maximum in contrast to 2TT-*m*C6B (816 nm) suggested the existence of twisted structure in 2TT-*m,o*C6B. Besides the absorption wavelength, molar extinction coefficient (ε) is also a key factor to determine the penetration depth. Based on the widespread use of 808 nm laser in biological applications, the ε at this wavelength was investigated. The ε of 2TT-*m, o*C6B (1.06×10^4 M^{-1} cm^{-1}) at 808 nm was significantly higher than that of 2TT-*o*C6B (0.53×10^4 M^{-1} cm^{-1}), even though slightly lower than that of 2TT-*m*C6B (1.4×10^4 M^{-1} cm^{-1}) (Supplementary Fig. S17). These data demonstrated the positive effect of planar architecture on the absorption efficiency. Then the photoluminescence (PL) property of the dyes was studied. As shown in Fig. 3b, their emission maxima in THF belonged to the NIR-II region, which was beneficial for high clarity fluorescence imaging. Notably, compared to the unimodal profile of 2TT-*o*C6B (1013 nm) and 2TT-*m*C6B (1070 nm), 2TT-*m, o*C6B displayed multimodal fluorescence spectrum ranging from 1000 to 1100 nm owing to the mixed planar and twisted structure. Since the dye molecules are normally in the form of aggregated state in life medium, their photophysical properties are thus investigated. Upon aggregation, a redshift in absorption maxima compared to the solution profile was observed for the three molecules owing to the intermolecular interactions (Fig. 3c) [49].

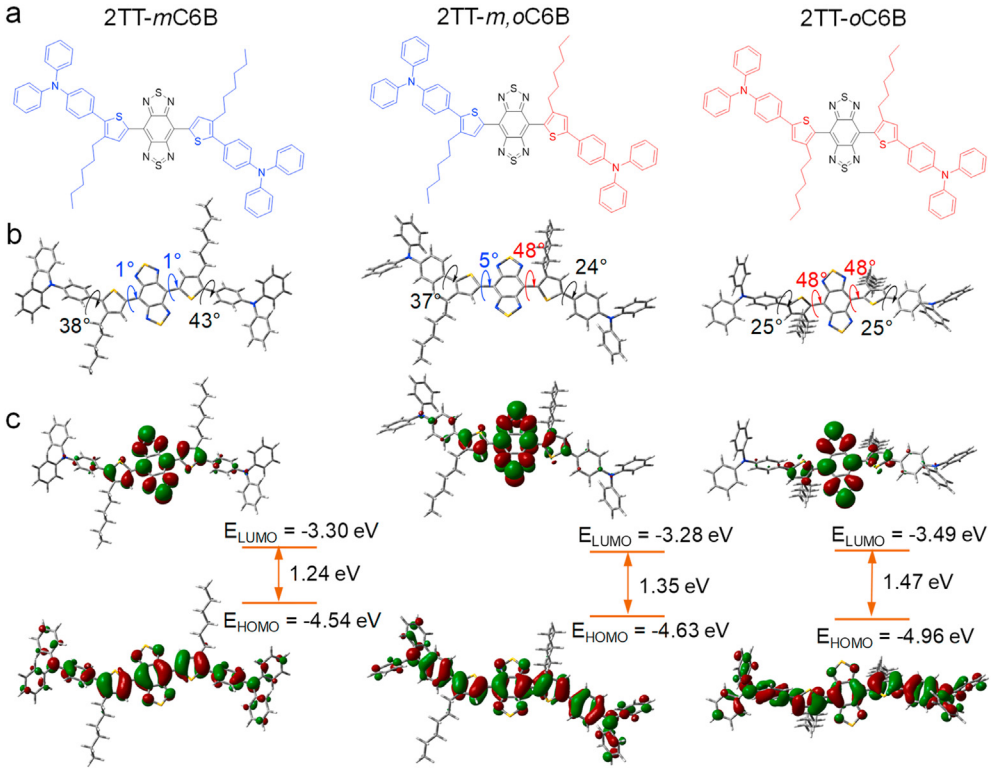

Fig. 2. Theoretical calculation data of 2TT-*m*C6B, 2TT-*m, o*C6B and 2TT-*o*C6B. (a) Chemical structures. (b) Molecular architectures and dihedral angles of the optimized S_0 geometries. (c) Calculated HOMOs and LUMOs of the molecules. The HOMO and LUMO energy levels and their gaps are also displayed. All the quantum mechanics calculations were performed by the Gaussian 09 program. The optimized conformations of these three compounds were calculated in the gas phase using B3LYP/6-311G (d,p) method. The frontier molecular orbitals of HOMO and LUMO were plotted with isovalue = 0.02.

For example, the 2TT-*m, o*C6B aggregate exhibited an absorption peak at 774 nm, a 24 nm redshift in comparison with the solution spectrum. Accompanied with the redshift of the absorption peak, the ε at 808 nm slightly increased to 1.12 $\times 10^4$ M^{-1} cm^{-1} for 2 TT-*m,o*C6B. Notably, 2TT-*m, o*C6B exhibited strong PL signal in the aggregated state with an emission peak at ~1050 nm (Fig. 3d).

To confirm the AIE or ACQ properties of 2TT-*m,o*C6B, the fluorescence intensity fluctuations of the molecules in THF/water mixtures with different water volume fractions (f_w) were investigated. As shown in Fig. 3e, the fluorescence signal was progressively weakened with the increase of f_w from 0% to 40%, due to the forming of twisted intramolecular charge transfer (TICT) state [50,51]. The TICT state goes back to the ground state mainly through the nonradiative decay, thus resulting in a decrease in fluorescence intensity [52–54]. Further increasing f_w to 90% gradually intensified the PL signal. These data demonstrated the typical AIE attribute of 2TT-*m,o*C6B, as a result of the restriction of intermolecular interactions by the half-twisted structure in the aggregated state and the suppression of the TICT state (Supplementary Fig. S18). α_{AIE} (PL intensity at $f_w = 90\%$ versus $f_w = 0$) is a factor that can distinguish the emission efficiency in the aggregated state. The α_{AIE} of 2TT-*m, o*C6B (1.13) was in between 2TT-*o*C6B (6.12) and 2TT-*m*C6B (0.06), suggesting its unique twisted/planar architecture (Fig. 3f). All these results are supportive that 2TT-*m, o*C6B with balanced absorption and emission could be promising for NIR-II fluorescence imaging.

3.4. In vitro imaging

In order to support 2TT-*m, o*C6B as an effective bio-agent, we fabricated water-soluble NPs through the nanoprecipitation method using biocompatible amphiphilic polymer DSPE-PEG_{2000} (Fig. 4a). Fabrication

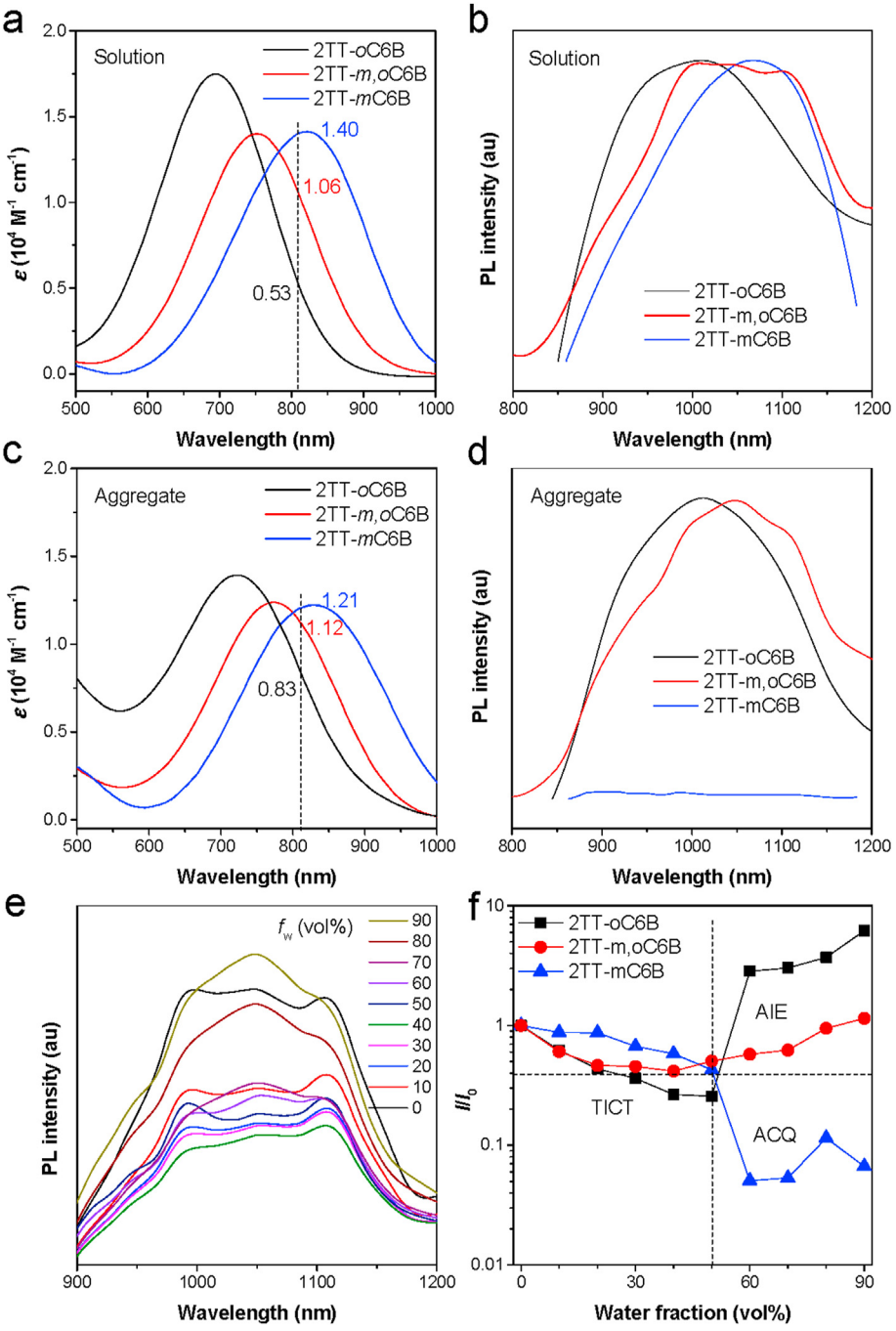

Fig. 3. (a) Molar absorption coefficient of molecules in THF. The concentrations for 2TT-*o*C6B, 2TT-*m, o*C6B and 2TT-*m*C6B are 1.74×10^{-4}, 1.40×10^{-4} and 1.41×10^{-4} mol L^{-1}, respectively. (b) Normalized PL spectra of molecules in THF. (c) Molar absorption coefficient of molecules in aggregate ($f_w = 90$ vol%, f_w refers to the water volume fraction in water/THF mixture). (d) Normalized PL spectra of molecules in aggregate (f_w = 90 vol%). (e) PL spectra of 2TT-*m, o*C6B (10^{-5} mol L^{-1}) in THF/H_2O mixture with different f_w. (f) Variation of PL intensity of the molecules (10^{-5} mol L^{-1}) with f_w.

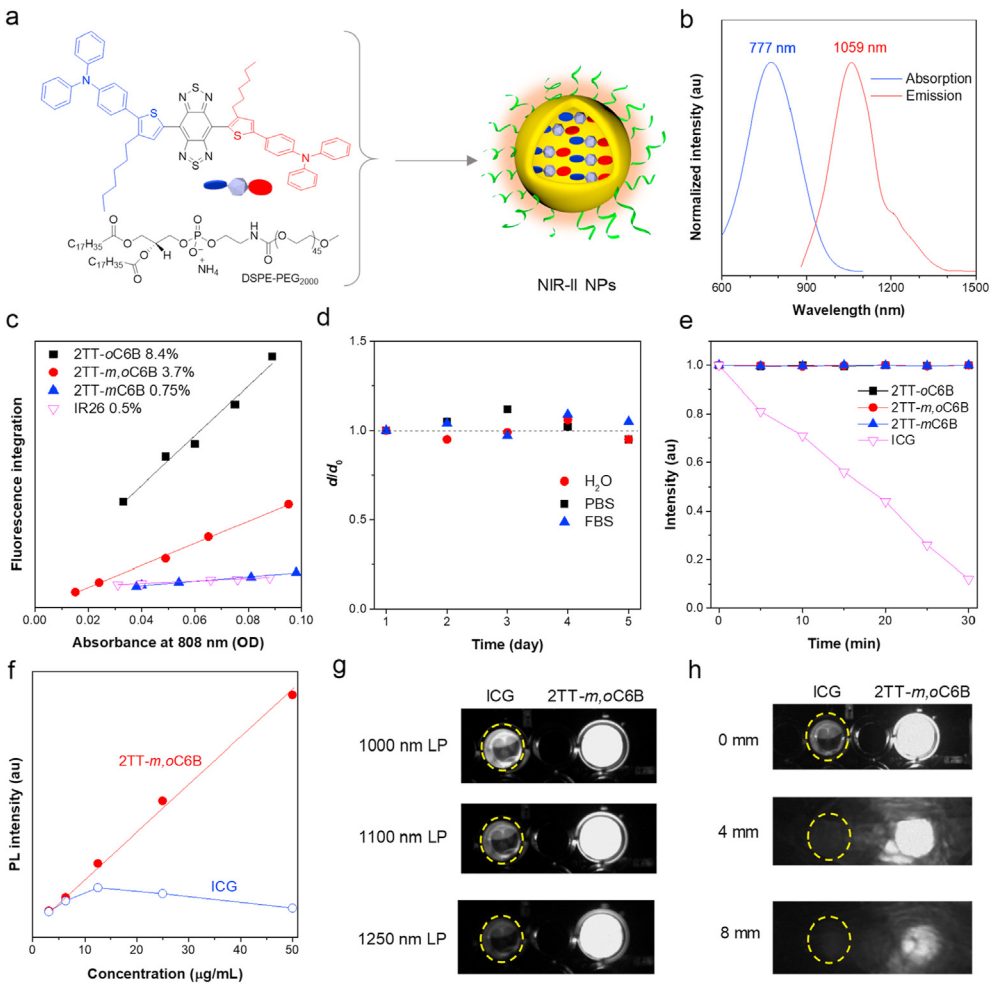

Fig. 4. Photophysical properties of 2TT-*m*, *o*C6B NPs. (a) Fabrication of 2TT-*m*, *o*C6B NPs using amphiphilic polymer DSPE-PEG_{2000}. (b) Normalized absorption and emission profile of 2TT-*m*, *o*C6B NPs. (c) The plots for the integrated fluorescence spectra (1000–1500 nm) of the sample nanoparticles and IR-26 (1000–1500 nm) at 5 different concentrations. (d) The colloidal stability of 2TT-*m*, *o*C6B NPs in H_2O, PBS and FBS, respectively. (e) Photostability of the 2TT-*m*, *o*C6B NPs versus ICG upon 808 nm laser irradiation (0.8 W/cm^2). (f) The relationship between fluorescence intensity and concentration for 2TT-*m*, *o*C6B NPs and ICG, respectively. (g) Comparison of brightness of 2TT-*m*, *o*C6B NPs and ICG (100 μg/mL) under 808 nm laser (20 mW/cm^2) using different LP filters (1000 nm, 50 ms; 1100 nm, 100 ms; 1250 nm, 200 ms). (h) Comparison of penetration depth of 2TT-*m*, *o*C6B NPs and ICG (100 μM based on 2TT-*m*, *o*C6B and ICG, 1250 nm LP filter, 800 ms, 20 mW/cm^2) under different thickness of chicken tissue.

of NPs with amphiphilic polymers is extremely valuable for biological applications, as they display excellent *in vivo* stability, biocompatibility, improved blood circulation time and passive tumor-targeting ability [55, 56]. Moreover, the resultant NPs trigger the fluorescence mechanism of AIE (restriction of intramolecular motion) to attain a strong fluorescence signal [57]. As shown in Fig. 4b, the 2TT-*m*, *o*C6B NPs (diameter of

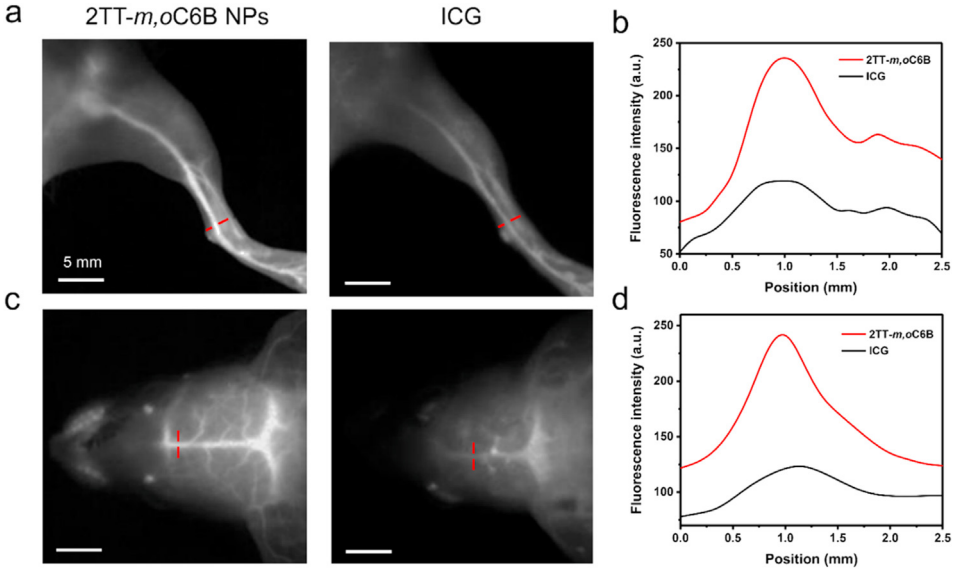

Fig. 5. NIR-II fluorescence imaging of blood vessels in (a) hindlimb and (c) brain at 5 min post-injection of 2TT-*m*, *o*C6B NPs and ICG (200 μL, 1 mM based on 2TT-*m*, *o*C6B and ICG), respectively (1250 nm LP filter, 500 ms, 20 mW/cm^2). (b,d) The fluorescence signal at the cross-section in hindlimb and brain (along the red-dashed line), respectively.

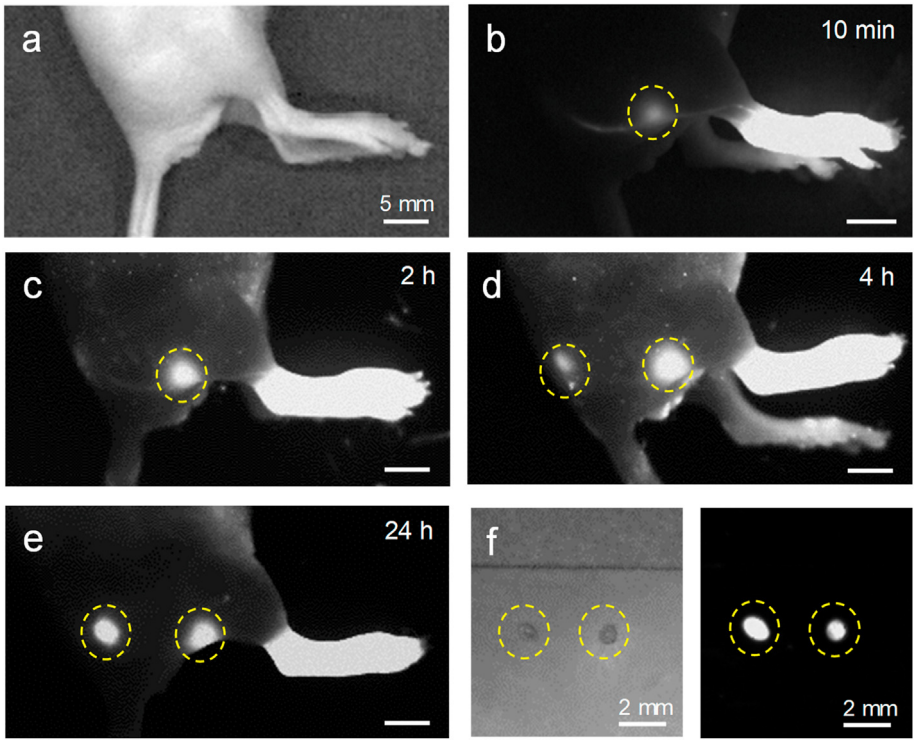

Fig. 6. *In vivo* NIR-II fluorescence imaging of the lymphatic system with 2TT-*m, o*C6B NPs (50 μL, 1 mM based on 2TT-*m,o*C6B, 1250 nm LP filter, 500 ms, 20 mW/cm^2). (a) Bright field. (b–e) Fluorescent field with images captured at 10 min, 2 h, 4 h, 24 h, respectively. (f) Bright (left) and fluorescent (right) images of sentinel lymph node extracted from the mouse under the guidance of NIR-II fluorescence.

~100 nm, Supplementary Fig. S19-20) showed intense absorption in the region of 600–900 nm with a peak at 777 nm, a 27 nm redshift compared to the solution-state spectrum. The 2TT-*m, o*C6B NPs exhibited PL emission maximum at 1059 nm with a tail extending to 1400 nm, which is capable of NIR-II imaging. The fluorescence QY of 2TT-*m, o*C6B NPs reached up to 3.7%, which was in the middle of 2TT-*m*C6B NPs (0.75%) and 2TT-*o*C6B NPs (8.4%) (Fig. 4c). The high QY for 2TT-*o*C6B NPs (8.4%) was resulted from the efficient suppression of intermolecular π-π interactions by twisted structures that facilitated the radiative decay pathway. While the low QY for 2TT-*m*C6B NPs (0.75%) was due to the predominant nonradiative decay from strong intermolecular π-π interactions of the planar structures. However, in 2TT-*m, o*C6B NPs, the moderate QY was owing to the balance of radiative and nonradiative decay from the twisted plus planar structure. These results indicated that we could precisely tune the photophysical properties of the dyes through structural modification. Moreover, 2TT-*m, o*C6B NPs displayed excellent

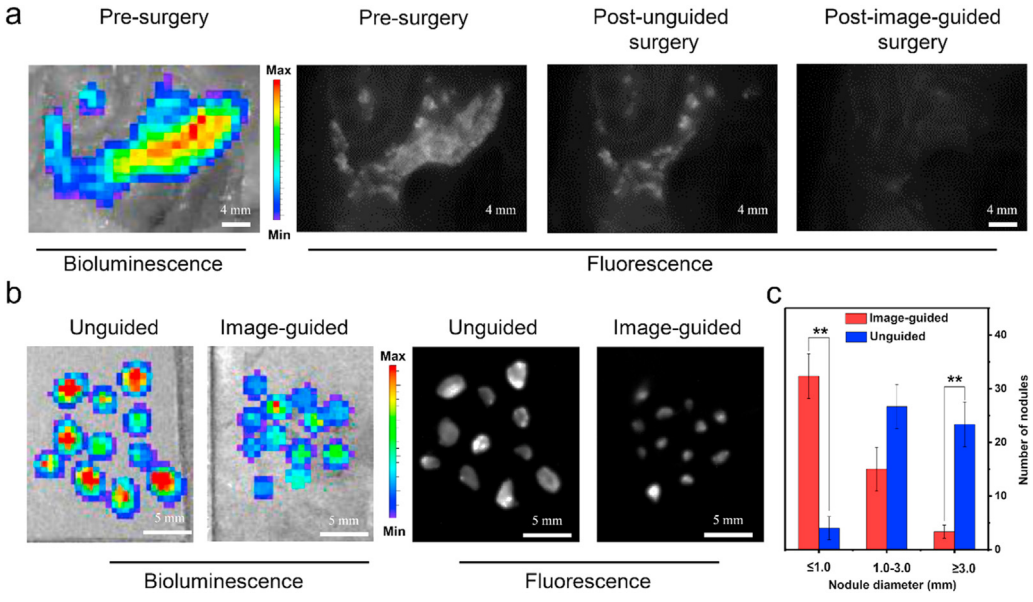

Fig. 7. Tumor resection with and without 2TT-*m, o*C6B NPs image-guided surgery (200 μL, 1 mM based on 2TT-*m,o*C6B, 1250 nm LP filter, 500ms, 20 mW/cm^2). (a) Bioluminescence and NIR-II imaging of the abdominal cavity before and after tumor resection. (b) Bioluminescence and NIR-II fluorescence signals of removed nodules of unguided and 2TT-*m, o*C6B NPs guided groups. (c) Histogram of nodules diameters resected from fluorescence guided and unguided groups (**$P < 0.01$, n = 3).

colloidal stability in different medium, such as water, phosphate-buffered saline (PBS) and fetal bovine serum (FBS) (Fig. 4d). It is crucially important for fluorescence dyes to maintain a reliable signal under different conditions. Thereof, we investigated the photostability of 2TT-*m, o*C6B NPs, while using the clinically approved indocyanine green (ICG) as a control. As shown in Fig. 4e, the PL intensity remained almost unchanged upon continuous laser irradiation (808 nm laser, 0.8 W/cm^2), while ICG displayed a rapid decrease in PL intensity with irradiation time. 2TT-*m, o*C6B also showed good photostability as molecular species (Supplementary Fig. S21). Moreover, the PL intensity of 2TT-*m, o*C6B NPs increased with the concentration, providing the potential platform for quantitative analysis (Fig. 4f). In contrast, the fluorescence intensity of ICG was slightly increased at low concentration but decreased at high concentration, displaying an ACQ effect. Furthermore, the *in vitro* NIR-II fluorescence signals of 2TT-*m, o*C6B NPs were evaluated. Under different LP filters (1000–1250 nm), 2TT-*m, o*C6B NPs displayed strong NIR-II signal even with 1250 nm LP filter, while feeble signals were observed in ICG (Fig. 4g), which was due to the superposition of the weaker NIR-II fluorescence of ICG and its ACQ effect. To attest the penetration depth, the NIR-II fluorescence signals of 2TT-*m, o*C6B NPs and ICG under different thickness of chicken tissues were detected (Fig. 4h). A high penetration depth of 8 mm was confirmed in 2TT-*m, o*C6B NPs, while the fluorescence signal of ICG could hardly be detected under 4 mm chicken tissue. All these data suggested the superb NIR-II imaging quality of 2TT-*m, o*C6B NPs than that of ICG.

3.5. Blood vessel imaging

Prior to blood vessel imaging, the *in vitro* cytotoxicity and *in vivo* toxicity of 2TT-*m, o*C6B NPs were assessed. Both results demonstrated the good biocompatibility of 2TT-*m, o*C6B NPs (Supplementary, Fig. S22-24). The *in vivo* pharmacokinetics of 2TT-*m, o*C6B NPs were also investigated using SD rats as the animal model. Figure S25 displays the blood clearance profile of 2TT-*m, o*C6B NPs with an elimination half-life of 7.59 ± 1.34 h. The other pharmacokinetic parameters were also calculated and summarized in Table S1. After confirming the good biocompatibility and long blood circulation time of 2TT-*m, o*C6B NPs, live mouse hindlimb and brain blood vessel imaging was performed through tail vein injection of agents to evaluate the *in vivo* imaging quality of 2TT-*m, o*C6B NPs. At 5 min post-injection, 2TT-*m, o*C6B NPs showed an improved resolution compared with ICG (Fig. 5a and c). Besides, with the decrease of the concentration of 2TT-*m, o*C6B NPs and ICG in the blood over time due to metabolism, the brightness of ICG in the blood vessels was always weaker than that of 2TT-*m, o*C6B NPs (Supplementary Fig. S26, 27). These results indicated that the NIR-II imaging quality of 2TT-*m, o*C6B NPs was still superior to that of ICG when the ACQ effect of ICG was removed. Moreover, even 8 h after administration, the blood vessels could be facilely identified, suggesting that 2TT-*m, o*C6B NPs are promising for long-term angiography. From the fluorescence signal at the cross-section of target vasculature, 2TT-*m, o*C6B NPs displayed much sharper PL spectra than that of ICG, attaining excellent clarity for *in vivo* imaging (Fig. 5b and d). The 2TT-*m, o*C6B NPs were found to be taken up by the mononuclear phagocytic system and to accumulate in the liver and spleen (Supplementary Fig. S28, 29). Altogether, benefited from the high fluorescence brightness of the NIR-II AIE dots, NIR-II fluorescence holds promise for high-resolution, real-time, deep-tissue and long-term vasculature visualization.

3.6. Image-guided lymph node surgery

Over the last few decades, the sentinel lymph node (SLN) hypothesis has proven feasible in selected types of cancer such as breast cancer, indicating that the pathological status of the first lymph node receiving the drainage directly from a tumor is sufficient to assess cancer metastasis [58–60]. SLN mapping has been extensively utilized in the intraoperative staging of many solid tumors, such as breast cancer and melanoma [61]. Recently, fluorescence imaging of lymph nodes has been extensively studied [62]. Owing to low autofluorescence and high photon penetration of NIR-II light, 2TT-*m, o*C6B NPs were considered for *in vivo* imaging of lymph nodes. As shown in Fig. 6a,50μL of 2TT-*m, o*C6B NPs (1 mM based on 2TT-*m,o*C6B) was subcutaneously injected into the footpads of nude mice. After 10 min of injection, 2TT-*m, o*C6B NPs migrated into the lymphatic vasculature and then lighted up the SLN (Fig. 6b). At 2 h of post-injection, the fluorescence signal at SLN intensified with the appearance of a second lymph node (Fig. 6c). Notably, the lymphatic duct between two lymph nodes could be visualized. The fluorescence signal in these two lymph nodes intensified with time and maximized at 24 h (Fig. 6d and e). Under the guidance of the NIR-II fluorescence, the SLNs with diameter less than 1 mm were precisely removed (Fig. 6f), which were validated by hematoxylin and eosin (H&E) histological staining (Supplementary Fig. S30).

3.7. Image-guided cancer surgery

Optical image-guided surgery has been proven efficient to improve surgery outcomes, which is demonstrated by some dyes such as ICG in patients [63–65]. However, the short blood circulation time, limited brightness and fast photobleaching of these dyes may result in unreliable guidance, especially for those tumors with small size (<1 mm). Alternatively, the high brightness, long blood circulation time and outstanding photostability of AIE NPs may provide a promising platform for surgical navigation.

In order to manifest the feasibility of 2TT-*m, o*C6B NPs to differentiate stubborn tumors, the peritoneal carcinomatosis-bearing mouse model was utilized owing to the presence of numerous tumor modules with various sizes in the peritoneal cavity. In general, it is hard to clinically identify and resect the submillimeter tumors, which may be a significant cause of cancer recurrence and metastasis [26,66]. To accurately track the tumor locations, 4T1 tumor cells expressing luciferase were injected intraperitoneally into mice, which afforded bioluminescence to tumor modules [67,68]. After the establishment of a mouse model, 2TT-*m, o*C6B NPs were administrated into mice via tail vein. At 24 h post-injection of 2TT-*m, o*C6B NPs (1 mM based on 2TT-*m,o*C6B, 200 μL), the mice were euthanatized and the abdomen cavity was opened for bioluminescence and NIR-II fluorescence imaging, respectively. As displayed in Fig. 7a, the fluorescence signal overlapped well with the bioluminescence signal, owing to the enhanced permeability and retention (EPR) effect and high-brightness of the NIR-II AIEgen NPs. Moreover, the strong NIR-II fluorescence signal permitted unambiguously delineate tiny tumors from the surrounding healthy tissues with a high tumor-to-normal tissue ratio of 10.1.

The application of 2TT-*m, o*C6B NPs for fluorescence-guided tumor resection was then studied. A surgeon was invited to operate. As displayed in Fig. 7a, without the guidance of the fluorescence signal, the surgeon removed lots of relatively large tumor nodules with diameters >1 mm based on his experience. Nevertheless, there were still many scattered fluorescence signals in the peritoneal cavity after the unguided surgery, indicating the remaining of tumor nodules. A second round of surgery was performed under the direction of NIR-II fluorescence signal to remove small tumor nodules. Under the high brightness of 2TT-*m, o*C6B NPs, the surgeon completely removed tumor nodules in fluorescence signal-guided surgery (Fig. 7a, right), which was confirmed by the bioluminescence photograph taken again after the operation, where no bioluminescence signal of tumor cells was seen (Figure S31). The bioluminescence and fluorescence signals of the removed nodules overlapped thoroughly (Fig. 7b), indicating the accuracy of the surgery, which was also confirmed by the H&E staining image of the resected tumor nodules (Supplementary Fig. S32). It should be noted that the surgeon resected significantly more small tumor nodules with diameter <1 mm than that of the unguided group (**$P < 0.01$, Fig. 7c), indicating enhanced surgery accuracy by NIR-II fluorescence.

4. Conclusions

We have successfully proposed an approach of designing Janus NIR-II fluorophores by introducing electronic donors with twisted and planar structures into two flanks of central electronic acceptor motif. On the one hand, the planar architecture gives the molecule excellent light-absorbing ability but suffers from fluorescence quenching effect when aggregated as a result of strong intermolecular π-π interactions. On the other hand, the twisted structure yields strong fluorescence emission in the aggregated state because of restriction of intermolecular interactions, however, a decrease in absorption is observed. Herein, as a proof-of-concept, Janus molecule 2TT-*m,* *o*C6B with both twisted and planar electronic donors was developed to regulate the absorption and emission properties. To our delight, the resulting 2TT-*m,* *o*C6B NPs inherited the merits of planar and twisted parent compounds, displaying strong absorption (ε of 1.12 ×10^4 M^{-1} cm^{-1} at 808 nm) and emission (NIR-II QY = 3.7% with an emission peak of 1050 nm) properties in the aggregated state. Thanks to the high QY and ε, 2TT-*m,* *o*C6B NPs have demonstrated outperformed *in vivo* imaging quality than the clinically used ICG. Notably, the 2TT-*m,* *o*C6B NPs helped surgeons to improve the surgical accuracy by delineating small lymph nodes or tumor nodulus. With insights from molecular design, NIR-II biomedical imaging with improved brightness is efficient for visualizing much deeper tissues compared to visible (400–680 nm) and NIR-I (700–900 nm) imaging owing to the reduced light scattering and autofluorescence. In addition to fluorescence imaging, the strong NIR light-absorbing ability may endow 2TT-*m,* *o*C6B NPs with excellent photothermal conversion properties, which may find applications in photoacoustic imaging, photothermal therapy (PTT), NIR-II fluorescence-guided PTT or seawater desalination. Overall, the present study provides a rational design strategy of establishing the structure-property relationship of NIR-II probes to control their emission and absorption properties.

Data availability statement

The data that supports the findings of this study are available within the article and its supplementary material.

Credit author statement

Shunjie Liu performed the experimental work, analyzed data and wrote the manuscript. Hanlin Ou and Ben Zhong Tang conceptualized the study and revised the manuscript. Yuanyuan Li, Jianquan Zhang, Haoke Zhang, Yong Wang, Clarence Chuah, Youhong Tang, Jacky W. Y. Lam, Ryan T. K. Kwok and Ding Dan participated the discussion. All authors approved the final version of the manuscript.

Declaration of competing interest

The authors declare that they have no known competing financial interests or personal relationships that could have appeared to influence the work reported in this paper.

Acknowledgments

We are grateful for the financial support from the National Natural Science Foundation of China, China (21788102, 31900983), the Research Grant Council of Hong Kong, Hong Kong (16305518 and C6009-17G), the Innovation and Technology Commission, Hong Kong (ITC-CNERC14SC01 and ITCPD/17–9), and National Key Research and Development Program of China, China (2018YFE0190200).

Appendix A. Supplementary data

Supplementary data to this article can be found online at https://doi.org/10.1016/j.mtbio.2020.100087.

References

[1] F. Bray, J. Ferlay, I. Soerjomataram, R.L. Siegel, L.A. Torre, A. Jemal, Global cancer statistics 2018: GLOBOCAN estimates of incidence and mortality worldwide for 36 cancers in 185 countries, CA Cancer J. Clin. 68 (2018) 394–424. https://doi.org/10.3322/caac.21492.

[2] J.D. Wulfkuhle, L.A. Liotta, E.F. Petricoin, Proteomic applications for the early detection of cancer, Nat. Rev. Canc. 3 (2003) 267–275. http://doi:10.1038/nrc1043.

[3] K.R. Kozak, F. Su, J.P. Whitelegge, K. Faull, S. Reddy, R. Farias-Eisner, Characterization of serum biomarkers for detection of early stage ovarian cancer, Proteomics 5 (2005) 4589–4596. https://doi.org/10.1002/pmic.200500093.

[4] S. Keereweer, J.D. Kerrebijn, P.B. Van Driel, B. Xie, E.L. Kaijzel, T.J. Snoeks, I. Que, M. Hutteman, J.R. Van der Vorst, J.S.D. Mieog, Optical image-guided surgery—where do we stand? Mol. Imag. Biol. 13 (2011) 199–207. https://doi.org/10.1007/s11307-010-0373-2.

[5] C. Chi, Y. Du, J. Ye, D. Kou, J. Qiu, J. Wang, J. Tian, X. Chen, Intraoperative imaging-guided cancer surgery: from current fluorescence molecular imaging methods to future multi-modality imaging technology, Theranostics 4 (2014) 1072. https://doi.org/10.7150/thno.9899.

[6] S. Zhu, R. Tian, A.L. Antaris, X. Chen, H. Dai, Near-infrared-II molecular dyes for cancer imaging and surgery, Adv. Mater. 31 (2019) 1900321, https://doi.org/10.1002/adma.201900321.

[7] S. He, J. Song, J. Qu, Z. Cheng, Crucial breakthrough of second near-infrared biological window fluorophores: design and synthesis toward multimodal imaging and theranostics, Chem. Soc. Rev. 47 (2018) 4258–4278, https://doi.org/10.1039/C8CS00234G.

[8] Y. Fan, S. Wang, F. Zhang, Optical multiplexed bioassays for improved biomedical diagnostics, Angew. Chem. Int. Ed. 58 (2019) 13208–13219, https://doi.org/10.1002/anie.201901964.

[9] L. Tu, Y. Xu, Q. Ouyang, X. Li, Y. Sun, Recent advances on small-molecule fluorophores with emission beyond 1000 nm for better molecular imaging in vivo, Chin. Chem. Lett. 30 (2019) 1731–1737, https://doi.org/10.1016/j.cclet.2019.05.022.

[10] C. Li, Q. Wang, Advanced NIR-II fluorescence imaging technology for in vivo precision tumor theranostics, Adv. Ther. 2 (2019) 1900053, https://doi.org/10.1002/adtp.201900053.

[11] S. Liu, Y. Li, R.T.K. Kwok, J.W.Y. Lam, B.Z. Tang, Structural and process controls of AIEgens for NIR-II theranostics, Chem. Sci. (2020). http://doi:10.1039/D0SC02911D.

[12] W. Xu, D. Wang, B.Z. Tang, NIR-II AIEgens: a win-win integration towards bioapplications, Angew. Chem. Int. Ed. (2020). http://doi:10.1002/anie.202005899.

[13] J. Huang, K. Pu, Activatable molecular probes for second near-infrared fluorescence, chemiluminescence, and photoacoustic imaging, Angew. Chem. 132 (2020) 11813–11827, https://doi.org/10.1002/anie.202001783.

[14] J. Cao, B. Zhu, K. Zheng, S. He, L. Meng, J. Song, H. Yang, Recent progress in NIR-II contrast agent for biological imaging, Front. bioeng. biotechnol. 7 (2020) 487, https://doi.org/10.3389/fbioe.2019.00487.

[15] Y. Duan, B. Liu Kenry, Recent advances of optical imaging in the second near-infrared window, Adv. Mater. 30 (2018) 1802394. http://doi:10.1002/adma.201802394.

[16] G. Hong, S. Diao, A.L. Antaris, H. Dai, Carbon nanomaterials for biological imaging and nanomedicinal therapy, Chem. Rev. 115 (2015) 10816–10906, https://doi.org/10.1021/acs.chemrev.5b00008.

[17] N.M. Bardhan, D. Ghosh, A.M. Belcher, Carbon nanotubes as in vivo bacterial probes, Nat. Commun. 5 (2014) 4918. http://doi:10.1038/ncomms5918.

[18] O.T. Bruns, T.S. Bischof, D.K. Harris, D. Franke, Y. Shi, L. Riedemann, A. Bartelt, F.B. Jaworski, J.A. Carr, C.J. Rowlands, M.W.B. Wilson, O. Chen, H. Wei, G.W. Hwang, D.M. Montana, I. Coropceanu, O.B. Achorn, J. Kloepper, J. Heeren, P.T.C. So, D. Fukumura, K.F. Jensen, R.K. Jain, M.G. Bawendi, Next-generation in vivo optical imaging with short-wave infrared quantum dots, Nat. Biomed. Eng. 1 (2017), 0056. http://doi:10.1038/s41551-017-0056.

[19] D. Naczynski, M. Tan, M. Zevon, B. Wall, J. Kohl, A. Kulesa, S. Chen, C. Roth, R. Riman, P. Moghe, Rare-earth-doped biological composites as in vivo shortwave infrared reporters, Nat. Commun. 4 (2013) 1–10. https://doi.org/10.1038/ncomms3199.

[20] G. Chen, T.Y. Ohulchanskyy, S. Liu, W.-C. Law, F. Wu, M.T. Swihart, H. Ågren, P.N. Prasad, Core/shell NaGdF4: Nd3+/NaGdF4 nanocrystals with efficient near-infrared to near-infrared downconversion photoluminescence for bioimaging applications, ACS Nano 6 (2012) 2969–2977, https://doi.org/10.1021/nn2042362.

[21] C. Chen, H. Ou, R. Liu, D. Ding, Regulating the photophysical property of organic/polymer optical agents for promoted cancer phototheranostics, Adv. Mater. 32 (2020) 1806331, https://doi.org/10.1002/adma.201806331.

[22] J. Qian, B.Z. Tang, AIE luminogens for bioimaging and theranostics: from organelles to animals, Inside Chem. 3 (2017) 56–91, https://doi.org/10.1016/j.chempr.2017.05.010.

[23] S. Kim, C.-K. Lim, J. Na, Y.-D. Lee, K. Kim, K. Choi, J.F. Leary, I.C. Kwon, Conjugated polymer nanoparticles for biomedical in vivo imaging, Chem. Commun. 46 (2010) 1617–1619, https://doi.org/10.1039/B923309A.

[24] H.-B. Cheng, Y. Li, B.Z. Tang, J. Yoon, Assembly strategies of organic-based imaging agents for fluorescence and photoacoustic bioimaging applications, Chem. Soc. Rev. 49 (2020) 21–31. http://doi:10.1039/C9CS00326F.

[25] L. Feng, C. Zhu, H. Yuan, L. Liu, F. Lv, S. Wang, Conjugated polymer nanoparticles: preparation, properties, functionalization and biological applications, Chem. Soc. Rev. 42 (2013) 6620–6633, https://doi.org/10.1039/C3CS60036J.

[26] Y. Sun, X. Zeng, Y. Xiao, C. Liu, H. Zhu, H. Zhou, Z. Chen, F. Xu, J. Wang, M. Zhu, Novel dual-function near-infrared II fluorescence and PET probe for tumor delineation and image-guided surgery, Chem. Sci. 9 (2018) 2092–2097, https://doi.org/10.1039/C7SC04774F.

[27] S. Liu, H. Zhang, Y. Li, J. Liu, L. Du, M. Chen, R.T.K. Kwok, J.W.Y. Lam, D.L. Phillips, B.Z. Tang, Strategies to enhance the photosensitization: polymerization and the donor–acceptor even–odd effect, Angew. Chem. Int. Ed. 57 (2018) 15189–15193. http://doi:10.1002/anie.201810326.

[28] Q. Yang, Z. Hu, S. Zhu, R. Ma, H. Ma, Z. Ma, H. Wan, T. Zhu, Z. Jiang, W. Liu, L. Jiao, H. Sun, Y. Liang, H. Dai, Donor engineering for NIR-II molecular fluorophores with enhanced fluorescent performance, J. Am. Chem. Soc. 140 (2018) 1715–1724. http://doi:10.1021/jacs.7b10334.

[29] S. Liu, C. Chen, Y. Li, H. Zhang, J. Liu, R. Wang, S.T.H. Wong, J.W.Y. Lam, D. Ding, B.Z. Tang, Constitutional isomerization enables bright NIR-II AIEgen for brain-inflammation imaging, Adv. Funct. Mater. 30 (2020) 1908125. http://doi:10.1002/adfm.201908125.

[30] H. Ma, C. Liu, Z. Hu, P. Yu, X. Zhu, R. Ma, Z. Sun, C.-H. Zhang, H. Sun, S. Zhu, Propylenedioxy thiophene donor to achieve NIR-II molecular fluorophores with enhanced brightness, Chem. Mater. 32 (2020) 2061–2069, https://doi.org/10.1021/acs.chemmater.9b05159.

[31] Y. Yamaguchi, Y. Matsubara, T. Ochi, T. Wakamiya, Z.-i. Yoshida, How the π conjugation length Affects the fluorescence emission efficiency, J. Am. Chem. Soc. 130 (2008) 13867–13869. http://doi:10.1021/ja8040493.

[32] J. Weiss, Fluorescence of organic molecules, Nature 152 (1943) 176–178. https://www.nature.com/articles/152176a0.

[33] Z. Zhao, H. Zhang, J.W.Y. Lam, B.Z. Tang, Aggregation-induced emission: new vistas at the aggregate level, Angew. Chem. Int. Ed. 59 (2020) 9888–9907. http://doi:10.1002/anie.201916729.

[34] Q. Li, Z. Li, Miracles of molecular uniting, Sci. China Mater. 63 (2020) 177–184. http://doi:10.1007/s40843-019-1172-2.

[35] N. Jiang, T. Shen, J.Z. Sun, B.Z. Tang, Aggregation-induced emission: right there shining, Sci. China Mater. 62 (2019) 1227–1235. http://doi:10.1007/s40843-019-9443-8.

[36] S. Xu, Y. Duan, B. Liu, Precise molecular design for high-performance luminogens with aggregation-induced emission, Adv. Mater. 32 (2020) 1903530. http://doi:10.1002/adma.201903530.

[37] H. Zhang, Z. Zhao, P.R. McGonigal, R. Ye, S. Liu, J.W.Y. Lam, R.T.K. Kwok, W.Z. Yuan, J. Xie, A.L. Rogach, B.Z. Tang, Clusterization-triggered emission: uncommon luminescence from common materials, Mater, Today Off. 32 (2020) 275–292, https://doi.org/10.1016/j.mattod.2019.08.010.

[38] Y. Li, S. Liu, T. Han, H. Zhang, C. Chuah, R.T.K. Kwok, J.W.Y. Lam, B.Z. Tang, Sparks fly when AIE meets with polymers, Mater. Chem. Front. 3 (2019) 2207–2220. http://doi:10.1039/C9QM00404A.

[39] S. Liu, Y. Li, H. Zhang, Z. Zhao, X. Lu, J.W.Y. Lam, B.Z. Tang, Molecular motion in the solid state, ACS Materials Lett 1 (2019) 425–431. http://doi:10.1021/acsmaterialslett.9b00292.

[40] S. Liu, Y. Cheng, Y. Li, M. Chen, J.W.Y. Lam, B.Z. Tang, Manipulating solid-state intramolecular motion toward controlled fluorescence patterns, ACS Nano 14 (2020) 2090–2098. http://doi:10.1021/acsnano.9b08761.

[41] S. Liu, H. Ou, Y. Li, H. Zhang, J. Liu, X. Lu, R.T.K. Kwok, J.W.Y. Lam, D. Ding, B.Z. Tang, Planar and twisted molecular structure leads to the high brightness of semiconducting polymer nanoparticles for NIR-IIa fluorescence imaging, J. Am. Chem. Soc. 142 (2020) 15146–15156. http://doi:10.1021/jacs.0c07193.

[42] S. Liu, R. Chen, J. Zhang, Y. Li, M. He, X. Fan, H. Zhang, X. Lu, R.T.K. Kwok, H. Lin, J.W.Y. Lam, J. Qian, B.Z. Tang, Incorporation of planar blocks into twisted skeletons: boosting brightness of fluorophores for bioimaging beyond 1500 nanometer, ACS Nano 14 (2020) 14228–14239. http://doi:10.1021/acsnano.0c07527.

[43] I. Guidlines, Revision on guidelines on limits of exposure to laser radiation of wavelengths between 400 nm and 1.4 μm, Health Phys. 79 (2000) 431–440. https://pubmed.ncbi.nlm.nih.gov/11007467.

[44] H. Wan, J.Y. Yue, S.J. Zhu, T. Uno, X.D. Zhang, Q.L. Yang, K. Yu, G.S. Hong, J.Y. Wang, L.L. Li, Z.R. Ma, H.P. Gao, Y.T. Zhong, J. Su, A.L. Antaris, Y. Xia, J. Luo, Y.Y. Liang, H.J. Dai, A bright organic NIR-II nanofluorophore for three-dimensional imaging into biological tissues, Nat. Commun. 9 (2018). http://doi:10.1038/s41467-018-03505-4.

[45] Y. Li, Z. Cai, S. Liu, H. Zhang, S.T.H. Wong, J.W.Y. Lam, R.T.K. Kwok, J. Qian, B.Z. Tang, Design of AIEgens for near-infrared IIb imaging through structural modulation at molecular and morphological levels, Nat. Commun. 11 (2020) 1255. http://doi:10.1038/s41467-020-15095-1.

[46] J. Du, S. Liu, P. Zhang, H. Liu, Y. Li, W. He, C. Li, J.H.C. Chau, R.T.K. Kwok, J.W.Y. Lam, L. Cai, Y. Huang, W. Zhang, J. Hou, B.Z. Tang, Highly stable and bright NIR-II AIE dots for intraoperative identification of ureter, ACS Appl. Mater. Interfaces 12 (2020) 8040–8049. http://doi:10.1021/acsami.9b22957.

[47] S. Liu, X. Zhou, H. Zhang, H. Ou, J.W.Y. Lam, Y. Liu, L. Shi, D. Ding, B.Z. Tang, Molecular motion in aggregates: manipulating TICT for boosting photothermal theranostics, J. Am. Chem. Soc. 141 (2019) 5359–5368. http://doi:10.1021/jacs.8b13889.

[48] Y. Li, Y. Liu, Q. Li, X. Zeng, T. Tian, W. Zhou, Y. Cui, X. Wang, X. Cheng, Q. Ding, X. Wang, J. Wu, H. Deng, Y. Li, X. Meng, Z. Deng, X. Hong, Y. Xiao, Novel NIR-II organic fluorophores for bioimaging beyond 1550 nm, Chem. Sci. 11 (2020) 2621–2626. http://doi:10.1039/C9SC06567A.

[49] N. Alifu, A. Zebibula, J. Qi, H.Q. Zhang, C.W. Sun, X.M. Yu, D.W. Xue, J.W.Y. Lam, G.H. Li, J. Qian, B.Z. Tang, Single-molecular near-infrared-II theranostic systems: ultrastable Aggregation-induced emission nanoparticles for long-term tracing and efficient photothermal therapy, ACS Nano 12 (2018) 11282–11293. http://doi:10.1021/acsnano.8b05937.

[50] R. Hu, E. Lager, A. Aguilar-Aguilar, J. Liu, J.W.Y. Lam, H.H.Y. Sung, I.D. Williams, Y. Zhong, K.S. Wong, E. Peña-Cabrera, B.Z. Tang, Twisted intramolecular charge transfer and aggregation-induced emission of BODIPY derivatives, J. Phys. Chem. C 113 (2009) 15845–15853. http://doi:10.1021/jp902962h.

[51] M. Borelli, G. Iasilli, P. Minei, A. Pucci, Fluorescent polystyrene films for the detection of volatile organic compounds using the twisted intramolecular charge transfer mechanism, Molecules 22 (2017) 1306. https://doi.org/10.3390/molecules22081306.

[52] Z.R. Grabowski, K. Rotkiewicz, W. Rettig, Structural changes accompanying intramolecular electron Transfer: focus on twisted intramolecular charge-transfer states and structures, Chem. Rev. 103 (2003) 3899–4032. http://doi:10.1021/cr940745l.

[53] D. Liese, G. Haberhauer, Rotations in excited ICT states – fluorescence and its microenvironmental sensitivity, Isr. J. Chem. 58 (2018) 813–826. http://doi:10.1002/ijch.201800032.

[54] S. Sasaki, G.P.C. Drummen, G.-i. Konishi, Recent advances in twisted intramolecular charge transfer (TICT) fluorescence and related phenomena in materials chemistry, J. Mater. Chem. C 4 (2016) 2731–2743. http://doi:10.1039/C5TC03933A.

[55] D. Ding, D. Mao, K. Li, X. Wang, W. Qin, R. Liu, D.S. Chiam, N. Tomczak, Z. Yang, B.Z. Tang, Precise and long-term tracking of adipose-derived stem cells and their regenerative capacity via superb bright and stable organic nanodots, ACS Nano 8 (2014) 12620–12631, https://doi.org/10.1021/nn505554y.

[56] G. Feng, B. Liu, Aggregation-induced emission (AIE) dots: emerging theranostic nanolights, Acc. Chem. Res. 51 (2018) 1404–1414. http://doi:10.1021/acs.accounts.8b00060.

[57] S. Liu, Y. Cheng, H. Zhang, Z. Qiu, R.T. Kwok, J.W. Lam, B.Z. Tang, In situ monitoring of RAFT polymerization by tetraphenylethylene-containing agents with aggregation-induced emission characteristics, Angew. Chem. Int. Ed. 57 (2018) 6274–6278, https://doi.org/10.1002/anie.201803268.

[58] L.M. Crane, G. Themelis, R.G. Pleijhuis, N.J. Harlaar, A. Sarantopoulos, H.J. Arts, A.G. van der Zee, N. Vasilis, G.M. van Dam, Intraoperative multispectral fluorescence imaging for the detection of the sentinel lymph node in cervical cancer: a novel concept, Mol. Imag. Biol. 13 (2011) 1043–1049. https://doi.org/10.1007/s11307-010-0425-7.

[59] S. Ohnishi, S.J. Lomnes, R.G. Laurence, A. Gogbashian, G. Mariani, J.V. Frangioni, Organic alternatives to quantum dots for intraoperative near-infrared fluorescent sentinel lymph node mapping, Mol. Imag. 4 (2005) 172–181, https://doi.org/10.1162/1535350200505127.

[60] N. Tagaya, R. Yamazaki, A. Nakagawa, A. Abe, K. Hamada, K. Kubota, T. Oyama, Intraoperative identification of sentinel lymph nodes by near-infrared fluorescence imaging in patients with breast cancer, Am. J. Surg. 195 (2008) 850–853, https://doi.org/10.1016/j.amjsurg.2007.02.032.

[61] R.W. Holloway, N.R. Abu-Rustum, F.J. Backes, J.F. Boggess, W.H. Gotlieb, W.J. Lowery, E.C. Rossi, E.J. Tanner, R.J. Wolsky, Sentinel lymph node mapping and staging in endometrial cancer: a Society of Gynecologic Oncology literature review with consensus recommendations, Gynecol. Oncol. 146 (2017) 405–415. https://doi.org/10.1016/j.ygyno.2017.05.027.

[62] M. Ankersmit, H. Bonjer, G. Hannink, L. Schoonmade, M. van der Pas, W. Meijerink, Near-infrared fluorescence imaging for sentinel lymph node identification in colon cancer: a prospective single-center study and systematic review with meta-analysis, Tech. Coloproctol. 23 (2019) 1113–1126. http://doi:10.1007/s10151-019-02107-6.

[63] Z. Hu, C. Fang, B. Li, Z. Zhang, C. Cao, M. Cai, S. Su, X. Sun, X. Shi, C. Li, T. Zhou, Y. Zhang, C. Chi, P. He, X. Xia, Y. Chen, S.S. Gambhir, Z. Cheng, J. Tian, First-in-human liver-tumour surgery guided by multispectral fluorescence imaging in the visible and near-infrared-I/II windows, Nat. Biomed. Eng. 4 (2020) 259–271. http://doi:10.1038/s41551-019-0494-0.

[64] C. Zeng, W. Shang, K. Wang, C. Chi, X. Jia, C. Fang, D. Yang, J. Ye, C. Fang, J. Tian, Intraoperative identification of liver cancer microfoci using a targeted near-infrared fluorescent probe for imaging-guided surgery, Sci. Rep. 6 (2016) 21959. https://doi.org/10.1038/srep21959.

[65] O.T. Okusanya, D. Holt, D. Heitjan, C. Deshpande, O. Venegas, J. Jiang, R. Judy, E. DeJesus, B. Madajewski, K. Oh, Intraoperative near-infrared imaging can identify pulmonary nodules, Ann. Thorac. Surg. 98 (2014) 1223–1230. https://doi.org/10.1016/j.athoracsur.2014.05.026.

[66] X. Ni, X. Zhang, X. Duan, H.-L. Zheng, X.-S. Xue, D. Ding, Near-infrared afterglow luminescent aggregation-induced emission dots with ultrahigh tumor-to-liver signal ratio for promoted image-guided cancer surgery, Nano Lett. 19 (2018) 318–330, https://doi.org/10.1021/acs.nanolett.8b03936.

[67] J. Qi, X. Duan, W. Liu, Y. Li, Y. Cai, J.W.Y. Lam, R.T.K. Kwok, D. Ding, B.Z. Tang, Dragonfly-shaped near-infrared AIEgen with optimal fluorescence brightness for precise image-guided cancer surgery, Biomaterials 248 (2020) 120036, https://doi.org/10.1016/j.biomaterials.2020.120036.

[68] X. Gu, X. Zhang, H. Ma, S. Jia, P. Zhang, Y. Zhao, Q. Liu, J. Wang, X. Zheng, J.W.Y. Lam, D. Ding, B.Z. Tang, Corannulene-incorporated AIE nanodots with highly suppressed nonradiative decay for boosted cancer phototheranostics in vivo, Adv. Mater. 30 (2018) 1801065. http://doi:10.1002/adma.201801065.